Rev. Roum. Sci. Techn.– Électrotechn. et Énerg.
Vol. **69**, *1*, pp. 109–114, Bucarest, 2024

FETAL 3D-ECHO CLASSIFICATION AND SEGMENTATION USING COLOR AND TEXTURAL FEATURES FOR TR DETECTION

MUTHUMANICKAM BHAGAVATHI PRIYA[1], CHANDRAN RAMAKRISHNAN[2], SUBBURATHINAM KARTHIK[3]

Keywords: Tricuspid regurgitation; Deep learning; Color-level co-occurrence Matrix; Grey-level co-occurrence Matrix; Independent component analysis.

Tricuspid regurgitation (TR) is a condition in which the valve between the right atrium and right ventricle does not close properly. Therefore, blood leaks backward into the upper right chamber. Most commonly, tricuspid regurgitation is caused by an enlarged right ventricle. In this paper, a novel deep learning technique called Tricuspid regurgitation identification in the fetal heart (TRI-FH) approach has been proposed, for identifying TR in the early stages. The gathered 3D-echo images are pre-processed to improve the quality of the images. The feature extraction techniques namely color-level co-occurrence matrix (CLCM) and grey-level co-occurrence matrix (GLCM) are applied on both RGB and grey images. The extracted features are extracted using the wrapper method and the unsupervised dimension reduction technique namely independent component analysis (ICA) is used to reduce the dimension of extracted features. Afterward, the deep learning-based Ghost network is used for classifying normal, Mild TR, and severe TR cases. The classified TR cases are fed to the segmentation phase for segmenting the affected valve of the fetus. The experimental TRI-FH approach achieves a total accuracy of 98.07 %. As compared to existing techniques, the proposed TRI-FH method shows higher performance in terms of accuracy, precision, recall, specificity, and F1 score. The proposed TRI-FH model enhances the total accuracy by 95.64 %, 97.82 %, 93.21 %, and 95.67 % better than ResNet, DenseNet, LinkNet, and U-Net respectively.

1. **INTRODUCTION**

TR is a common valve heart condition that develops with age, regardless of gender. Significant TR is expected to affect up to 2.7 % of patients, with the elderly being the most sensitive [1]. The tricuspid valve controls blood flow between the right atrium and the right ventricle. TV limits retrograde blood flow during systole but permits deoxygenated blood to move from RA to RV during diastole. For the television to function properly overall, these sub-valvular parts must function at their optimum. TR is a disease in which the function or architecture of the TV alters, reducing the overall efficiency of the RV function [2]. Numerous trials have demonstrated that delaying TR treatment during left-sided valve surgery causes TR to worsen and increases the risk of death [3]. Patients having surgery on their left-side valves for high-grade TR have been shown to live much longer after undergoing tricuspid valve intervention during that operation [4]. One of the most important clinical procedures [5] in contemporary clinical settings is gaining valve morphology based on CT images, which have outstanding information and spatial resolution on the interaction with surrounding structures, for the planning of treatment for aortic valve illness. To extract information about valve shape from CT images [6], however, radiologists and doctors must put in a lot of effort and spend considerable time. Because it provides 3D data with a high spatial resolution, CT imaging is the most effective tool for assessing TV and TR patients' remodeling of the right chambers. The fundamental mechanism of TR can be clarified by CT imaging [7], which can also be used to plan TV interventions and assess the anatomical compatibility of current transcatheter devices. A little TR will increase the inferior pressure to a point where the flow can be reversed when the RA is low, or the systemic venous pressure is high [8]. The connection between TA dilatation and TR is widely known. TR is detected early and sensitively by TA dilation and right and left atrial hypertrophy. Before RV dilatation, which eventually happens and is connected to more severe TR, the right atrial enlargement develops [9]. The clinical entity known as atrial functional tricuspid regurgitation in the situation of atrial fibrillation is more frequently considered to have distinctive echocardiographic evidence of annular dilatation associated with right atrial enlargement [10]. The overall severe TR population would almost definitely include a sizable fraction of the probable CAVI population. As a result, CAVI should be considered as a potentially viable alternative as more data become available for a variety of severe TR patients who face a high or prohibitive surgical risk [11]. The degree of regurgitation of the tricuspid valve was measured using the suggestions. The systolic pulmonary arterial pressure was estimated using the maximal TR jet velocity and the inferior vena cava respiratory variation. [12-16]. In this paper, a novel deep learning technique called Tricuspid Regurgitation Identification in Fetal Heart (TRI-FH) approach has been proposed, for identifying TR in the early stages. The main contribution of the research is as follows,

- The 3D-echo images are pre-processed to increase their quality. Both RGB and grey images can be processed using the feature extraction methods CLCM and GLCM.
- The extracted features are extracted using the wrapper method and the unsupervised dimension reduction technique namely Independent Component Analysis (ICA) used to reduce the dimension of extracted features. Then, the deep learning-based Ghost network is used for classifying normal, Mild TR, and severe TR cases.
- The classified TR cases are fed to the segmentation phase for segmenting the affected valve of the fetus.

The remaining sections of this work were split up into the five categories listed below. Section 2 presents the literature review; section 3 suggests the TRI-FH approach; section 4 presents the results and discussion, and section 5 presents the conclusion and suggestions for further work.

2. **LITERATURE SURVEY**

Tricuspid regurgitation is mostly caused by an enlarged right ventricle. The ventricles expand as a result of heart conditions, such as heart failure, pulmonary hypertension, and cardiomyopathy. A summary of a few of those study papers is provided in this section.

[1] Dr. Mahalingam College of Engineering and Technology, Pollachi India. Corresponding author: Bhagavathipriyam@drmcet.ac.in
[2] SNS College of Technology, Coimbatore, 641035 India. E-mail: ramakrishnan.c.eee@snsct.org
[3] SNS College of Technology, Coimbatore, 641035 India. E-mail: deancse@snsct.org

DOI: 10.59277/RRST-EE.2024.69.1.19

Reference [17] suggested a CNN detect structural abnormalities and cardiac substructures in fetal ultrasound films, cross-sections around four-chamber views, and images of the trachea with three vessels. SONO accuracy curve in the heart and vessels was 78.7 % and 89.1 %, respectively.

Reference [18] has created two of these strategies in an improved algorithm that can more accurately classify regurgitation forms and distinguish between classes with abnormalities and those without. Used deep learning approaches to classify regurgitation better than a well-known SVM method. It will reduce money while also assisting with early detection and diagnosis.

Reference [19] an ARV-based V-Net architecture can take a fetal cardiac rhabdomyoma segmentation. The main objective of developing an algorithm to automatically identify FCRD from ultrasound images has been achieved. fetal rhabdomyomas adjacent to the tricuspid valve, left ventricle, right ventricle, left atrium, and right atrium were treated with this technique.

Reference [20] developed an automated machine learning-based system for detecting and diagnosing echo regurgitation from video files. The extraction of video frames from a video file, results in a considerable reduction in the total number of frames. The method gives an overall accuracy of 95.33 %.

Reference [21] suggested an AI PIV based on DL and CNN that provides a high-resolution image of velocity fields. The right heart was captured using agitated saline bubble echocardiography in this innovative approach. These difficulties were overcome when higher-resolution data showed significant patterns and vortices throughout the cardiac cycle.

Reference [22] proposed to identify TVD cases and collect data, utilizing a single prenatal ultrasound clinic's trustworthy sonographic computerized database. The four-chamber view and valve color mapping of sonography were used to diagnose TVD. To rule out any other heart anomalies, a full fetal echocardiogram was performed.

Reference [23] had generated A-FTR is a clinical entity with distinct clinical care demands and TV intervention opportunities, as well as results that are anticipated to differ from V-FTR. For in-patient treatment and TTVI selection, it is essential to understand the etiology of FTR and be able to differentiate between A-FTR and V-FTR.

Reference [24] suggested Right atrial enlargement atrial functional TR is still not fully grasped. The existence of lone atrial fibrillation is the situation in which AF-TR is most frequently discovered, however it can also be. It is advised that physicians become more aware of this emerging clinical entity using this suggestion technique.

Reference [25] developed a deep learning-based technique for detecting and evaluating echo Doppler flows. This approach was trained using labeled images of real-world clinical variance. The proposed overall accuracy was 91.6 % and 88.9 %, respectively.

Reference [26] presented a meta-analysis that demonstrates the effectiveness of TAVI in BAS patients who are not candidates for surgery. Individuals with BAS experience stroke, conversion to surgery, second valve implantation, and paravalvular leak more frequently than patients with TAS and these risks must be communicated with the patient at every stage of the decision-making process.

The existing techniques do not handle any kind of fetal presentation. There is no way to exclude it from the pooled estimates, and the evidence is very ambiguous in the preceding sample, no studies with surgically low-risk patients were included in the meta-analysis. To overcome the above problem, we use fetal 3D-echo images to identify the TR cases immediately.

3. PROPOSED METHOD

In this section, the gathered 3D-echo images are pre-processed to improve the quality of the images. The feature extraction techniques namely CLCM and GLCM are applied on both RGB and grey images. The extracted features are extracted using the wrapper method and the unsupervised dimension reduction technique namely independent component analysis (ICA) used to reduce the dimension of extracted features. Afterward, the deep learning-based ghost network is used for classifying normal, Mild TR, and severe TR cases. The classified TR cases are fed to the segmentation phase for segmenting the affected valve of the fetus (Fig. 1). The overall workflow of the proposed TRI-FH model. Image reaping techniques are used to consider the area of vision for some further investigation. Using this method, the zone outside the area of attention is removed. To perform the picture-reaping procedure, a cover that defines the field of vision is constructed. The four extreme coordinates are obtained using this mask. Using these coordinates, the image is dynamically resized to the suitable width and height. Figure 2 shows input into the reaping image.

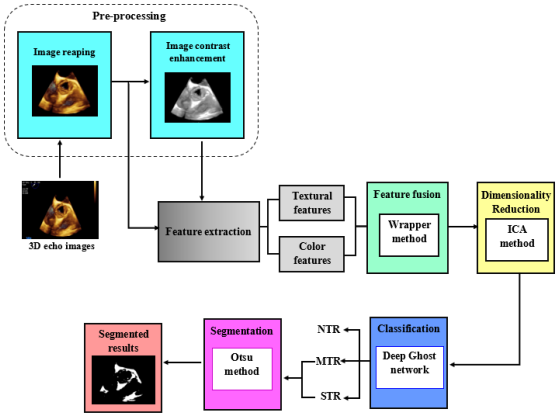

Fig 1 – The overall workflow of the Proposed model.

3.1. IMAGE REAPING

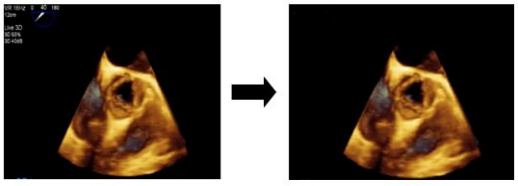

Input image Reaping image

Fig. 2 – Reaping image.

The phase discards approximately 40,000 pixels from drive fundus images with dimensions of 584×565 pixels. The value changes based on the size of the images field of vision. As a result, the image size is reduced and fewer pixels are probed in subsequent computations, lowering computational complexity. The color modification is done after the image has been cropped.

3.2. BILATERAL FILTER

The 3D-echo images are pre-processed by enhancing the

contrast using a bilateral filter. It can be used to reduce noise while maintaining edge detail by more carefully choosing which pixels go into the weighted total. According to pixels, the bilateral weights are computed. The advantage is preserved through this technique. This can be written as follows mathematically:

$$J'(y,z) = N_{bilateral}(y,z) \cdot$$
$$*\sum_{n=-3_{\sigma_1}}^{3\sigma_1} \sum_{m=-3_{\sigma_1}}^{3\sigma_1} K_{bilateral}\,(y,z,n,m) I(y+n, z+m), \quad (1)$$

where $N_{bilateral}$ is the normalization factor and $K_{bilateral}$ are the weights of each pixel in the filter region. It employs $K_{Gaussian}(n,m)$ is a collection of Gaussian weights function and a photometric exclusion function are multiplied to create the weighted total selective inclusion of image pixels $f_{edge}(y,z,n,m)$ to obtain the bilateral weight calculation function,

$$K_{bilateral}(y,z,n,m) = $$
$$= K_{Gaussian}(n,m) f_{edge}(y,z,n,m). \quad (2)$$

Differences in intensity are inversely related to the photoelectric exclusion function. A value close to zero is therefore returned by the photometric exclusion function if there is a significant intensity difference between the focused pixel at coordinates (y, z) and a pixel within the filter region at coordinates (y+n, z+m),

$$f_{edge}(y,z,n,m) = \mathrm{e}^{-\frac{(J(y+n,z+m)-J(y,z))^2}{2\sigma_2^2}}, \quad (3)$$

where σ_2 is a scaling factor J (y, z) is a contributing pixel. J (y+n, z+m) are the opposite sides of an edge. The scaling factor σ_2 indicates an intensity difference between the contributing and focused pixels that identifies them as being on the same side of an edge. $N_{bilateral}$ is a normalizing factor. In this process, bilaterally weighted intensities are averaged. $N_{bilateral}$ is given by

$$N_{bilateral}(y,z) = \frac{1}{\sum_{n=-3\sigma_1}^{3\sigma_1} \sum_{m=-3\sigma_1}^{3\sigma_1} K_{bilateral\,(y,z,n,m)}}. \quad (4)$$

Smoothing is done in an area with edges by only employing pixels that are adjacent to the focal pixel.

3.3. GLCM

GLCM for extracting the textural features in the images. Each item (m, n) in the GLCM represents the number of examples of the pair of grey levels m and n that are separated by d in the original image:

$$Q(m,n,d,\theta) = \#\{[(y,z),(y+d,z+d)|f(y,z) = $$
$$= m, f(y+d,z+d) = n]\}, \quad (5)$$

where θ represents the pixel's direction in space. Normalize the GLCM matrix before obtaining the features. The method is as follows:

$$Q(m,n,d,\theta) = Q(m,n,d,\theta)/S, \quad (6)$$

where S is standardized constant that represents the sum of (m, n). The six features mentioned below were utilized by their functions.

1. Energy, is also known as angular second moment, is a measure of an image's textural consistency.

$$W_1 = \sum_{m=0}^{i-1} \sum_{n=0}^{i-1} Q^2\,(m,n,d,\theta). \quad (7)$$

2. Entropy, a measurement of image disorder, reaches its maximum when all components of a matrix are equal

$$W_2 = -\sum_{m=0}^{i-1} \sum_{n=0}^{i-1} Q(m,n,d,\theta) \cdot$$
$$\cdot \log_{10} Q(m,n,d,\theta). \quad (8)$$

3. Contrast

$$W_3 = \sum_{m=0}^{i-1} \sum_{n=0}^{i-1} [(m-n)^2 \cdot Q^2(m,n,d,\theta). \quad (9)$$

The number of local deviations in an image is measured by contrast, which is the difference moment of the matrix.

4. Dissimilarly

$$W_4 = \sum_{m=0}^{i-1} \sum_{n=0}^{i-1} (m-n) \cdot Q(m,n,d,\theta). \quad (10)$$

5. Inverse difference moment

$$W_5 = \frac{\sum_{m=0}^{i-1} \sum_{n=0}^{i-1} Q\,(m,n,d,\theta)}{[1+(m-n)^2]}. \quad (11)$$

The inverse difference moment quantifies an image's homogeneity. When the majority of GLCM occurrences are located along the main diagonal, this parameter has the maximum value.

6. Variance

$$W_6 = \sum_{m=0}^{i-1} \sum_{n=0}^{i-1} (m-a)^2\ Q(m,n,d,\theta). \quad (12)$$

The variance represents the texture cycle, while an is the average value of $Q(m,n,d,\theta)$.

3.4. CLCM

GLCM is used to extract color characteristics from images. CLCM operates by altering four fundamental GLCM equations to extract the color texture description directly from a color image. CLCM probability matrices were defined using the equations below.

$$Pc_a, c_b, d, \theta\ (\text{diff}) = \#\{((i,j,c_a),(u,v,c_b))(L_y * L_x) \cdot$$
$$\cdot (L_y \cdot L_x) | (i-u=0, |j-v| = d)\}, \quad (13)$$
$$Pc_a, c_b, d, \theta(\text{diff}) = \#\{((i,j,c_a),(u,v,c_b)) \in (L_y \cdot L_z) \cdot$$
$$\cdot (L_y \cdot L_x) | (i-u=d, j-v=-d) \text{ or}$$
$$(i-u=-d, j-v=d)\}, \quad (14)$$
$$Pc_a, c_b, d, \theta(\text{diff}) = \#\{((i,j,c_a),(u,v,c_b))(L_y \cdot L_z) \cdot$$
$$(L_y \cdot L_z)(|i-u| = d, j-v=0)\}, \quad (15)$$
$$Pc_a, c_b, d, \theta(\text{diff}) = \#\{((i,j,c_a),(u,v,c_b)) \in (L_y \cdot L_z) \cdot$$
$$(L_y \cdot L_z) | (i-u=d, j-v=d) \text{ or}$$
$$(i-u=-d, j-v=-d)\}, \quad (16)$$
$$Pc_a, c_b, d, \theta(\text{diff}) = \#\{((i,j,c_a),(u,v,c_b))(L_y \cdot L_z) \cdot$$
$$(L_y \cdot L_z) | (i-u=0, j-v=0)\}, \quad (17)$$
$$\text{diff} = R(i,j,c_a) - R(u,v,c_b). \quad (18)$$

The $Pc_a, c_b, d, \theta(\text{diff})$ are the probability vectors, diff is the intensity value difference between two pixels in various colour channels. The symbol # represents the number of items in the set, and the characters d and denote the distance and angle between two pixels in an image, respectively. The sets of resolution cells of the color image components, organized by row-column identifiers, are expressed by $L_y \cdot L_z$. Then, $R(i,j,c_a)$ and $R(u,v,c_b)$ are intensities on position i, j, or u, v, of image R and c_a, c_b are color components of the image.

3.5. WRAPPER METHOD

The wrapper method is used to fuse the extracted features (color and texture). The wrapper fusion technique is frequently employed to maintain accuracy while minimizing computer complexity. To evaluate the caliber of the selected attributes, the wrapper-based models employ learning techniques. Most of the time, a search strategy in the space of potential feature subsets is predefined, and several feature subsets are generated and assessed.

3.6. INDEPENDENT COMPONENT ANALYSIS (ICA)

It is a generally used technique to extract features and reduce the dimensions. When the ICA method is used to extract image features, it separates images and produces a collection of independent source images. It then uses the above collection of independent source images as a set of base images for the image set, allowing the image set to be constructed from these

independent base images. The image's linear superposition under different combination coefficients reduces the redundancy of the pixel's grey value and isolates the important image elements. Figure 3 shows the ICA diagram.

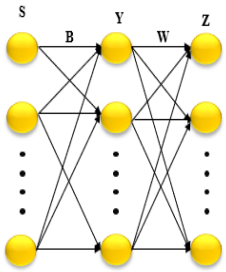

Fig 3 – ICA diagram.

Let $\mathbf{s} = [s_1, s_2, \ldots . s_n]^{\mathrm{T}}$ be n is an independent source signals with zero-mean value, and $\mathbf{Y} = [y_1, y_2, \ldots . y_m]^{\mathrm{T}}$ are m is a random observation signal.

$$\mathbf{Y} = \mathbf{BS}, \tag{19}$$

$$y_j = \sum_{k=1}^{n} b_{jk} s_j. \tag{20}$$

Among them, j = 1,2,… n, k = 1,2,… m, $\mathbf{B} = [b_1, b_2, \ldots . , b_n]$ is a full-rank matrix of n×m. Let $\mathbf{Z} = [z_1, z_2, \ldots . , z_m]$ be the estimated signal, then

$$\mathbf{Z} = \mathbf{WS} = \mathbf{WBS}. \tag{21}$$

The estimated signal is an independent source signal, while **W** and **WB** are the unmixing matrix and identity matrix, respectively.

3.7. DEEP GHOST NETWORK

The deep learning-based ghost network is used for classifying the cases. The ghost net model is used for fine-grained cervical cells. The discriminative power of light-weight convolutional neural networks utilized in cervical cell categorization was improved by applying a hybrid loss function with label smoothing. The primary ghost module divides the initial convolutional layer into two halves and uses fewer filters to provide a lot of intrinsic feature mappings. The successful generation of ghost feature maps can thus be accomplished using a small number of accessible transformation techniques. Figure 4 shows the architecture of ghost network.

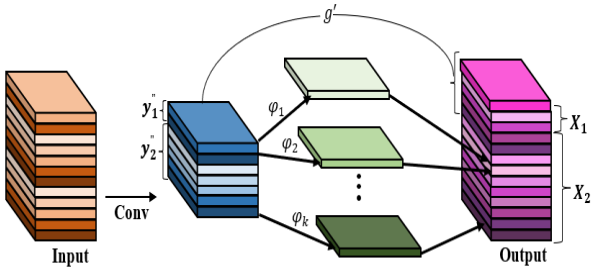

Fig. 4 – Architecture of ghost network.

Assume $y'' = y_1'' + y_2''(y_1'' < y_2''), y_1''$ and y_2'', where represent the basic feature information and redundant basic feature information, respectively. X_1 is generated using n intrinsic feature maps using y_1''. For each intrinsic feature map, linear operation ϕ_i is used to generate k ghost feature maps. So, n intrinsic feature maps are generated $m = n \cdot k$ ghost feature maps X_2. The n+m output convolution operation is displayed after the ghost convolution procedure, as follows:

$$X_1 = y_1'' \cdot g'$$

$$X_2 = y_{ij} = \varphi_i(x_i), \forall j = 1, \ldots . , n, i = 1, \ldots . , k \tag{22}$$

$$X = X_1 \cdot X_2,$$

where $g' \in T^{e*k*k*n}$ is the filter, k×k is the convolutional kernel size, n is the number of intrinsic feature maps $X_1 \in T^{h'w'm}$, $w'$and $h'$are the output feature maps breadth and height, and m is the number of ghost feature maps.

3.8. OTSU METHOD

The Otsu method and it's used in image segmentation, as well as the development of an improved threshold image segmentation algorithm, are discussed. The proper threshold should be chosen by maximising the weighted total of foreground and background pixel between-class variances, according to this procedure. The images into two classes are $Z_1$and Z_2 can be computed as,

$$\mu_{z_1} = \sum_{j=0}^{M} \frac{j*S_i}{S_{z_i}}, \tag{23}$$

$$\mu_{z_1} = \sum_{j=M+1}^{N-1} \frac{j*S_i}{S_{z_i}}. \tag{24}$$

So can get the equivalent formula:

$$\sigma^2(M) = S_{z_1} S_{z_2} (\mu_{z_1} - \mu_{z_2})^2. \tag{25}$$

The optimal threshold M^*can be produced by increasing the difference in variance between classes.

$$M^* = \mathrm{Arg} \max_{0<M<N-1} \sigma^2(T). \tag{26}$$

Since it is simple and has a reliable attachment, the Otsu approach has been extensively used in the segmentation of genuine images.

Both background noise and target size are very sensitive to it. After testing it out on a variety of photo types, it was found that it works best on images having a single peak variance. When there is a large difference between the two intra-class variances, the Otsu method's threshold tends to be closer to the class with the greater intra-class variation, indicating that more pixels from this class will be recognized as belonging to another class. As a result, the segmentation result must be improved.

4. RESULTS AND DISCUSSIONS

In this section, the proposed TRI-FH approach used for identifying TR in the early stages. Recall, accuracy, specificity, and precision are the metrics used to evaluate it. Various aspects are considered in evaluating the effectiveness of the model provided. Figure 5 shows the identifying of the TR cases. The proposed TRI-FH approach used for classifying normal, Mild TR and Severe TR cases. The input 3d echo images are gathered in column 1. The image reaping results are in column 2. Then, the pre-processed using Bilateral filter by improve the quality of the images are column 3. The extracted features are extracted images are column 4. Afterwards, the classifying results are normal, Mild TR and Severe TR cases are column 5. The experimental result of the proposed TRI-FH approach images is in column 6.

4.1. PERFORMANCE ANALYSIS

In this paper, the performance analysis was calculated based on specificity, accuracy, recall, precision, and F1 score,

$$\mathrm{Acuracy} = \frac{\mathrm{TP+TN}}{\mathrm{TP+TN+FP+FN}} \tag{27}$$

$$\mathrm{Precision} = \frac{\mathrm{TP}}{\mathrm{TP+FP}}, \tag{28}$$

$$\mathrm{Recall} = \frac{\mathrm{TP}}{\mathrm{TP+TN}}, \tag{29}$$

$$\mathrm{Specificity} = \frac{\mathrm{TN}}{\mathrm{TN+FP}}, \tag{30}$$

$$\mathrm{F1\ score} = 2\left(\frac{\mathrm{Precision*Recall}}{\mathrm{Precision+Recall}}\right), \tag{31}$$

where TN, FN represents the true and false negatives and TP, FP denotes the true and false of the sample fabrics.

Table 1
Performance analysis of the proposed TRI-FH model

Class	Accuracy	Specificity	Precision	Recall	F1 Score
Normal TR	97.53	96.63	95.32	93.54	91.47
Mild TR	96.26	94.28	93.46	92.63	90.38
Severe TR	95.42	93.58	94.61	93.82	93.17

Table 1 displays the classification of various TR classes according to specific parameters. The TRI-FH approach's average accuracy, F1 score, precision, recall, and specificity when used with the given parameters. The proposed TRI-FH approach has an average accuracy of 97.53 %, 96.26 %, and 95.42 %, respectively. The Proposed TRI-FH approach has acquired high accuracy in both training and testing accuracy, as shown in Fig. 6. The performance is based on the specificity, recall, accuracy, precision, and F1 score, as well as the accuracy obtained by the proposed model. According to the results, the classification accuracy of the Proposed TRI-FH approach was 98.07 %, respectively.

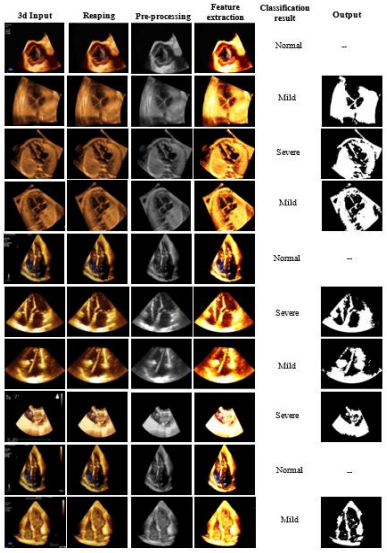

Fig 5 – Experimental result of the proposed TRI-FH model

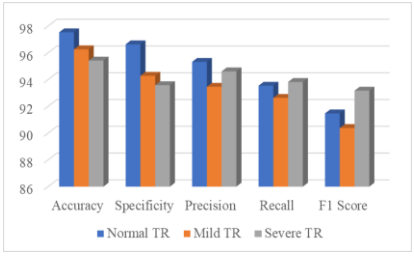

Fig. 6 – Performance metrics for three classes.

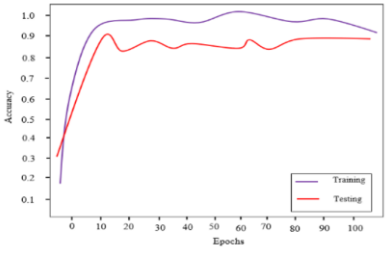

Fig. 7 – Training and testing accuracy curve of the proposed TRI-FH model.

The accuracy of the method increases as the number of epochs is raised, Fig. 7 shows the accuracy curve, which has accuracy and epochs on opposite axes. The loss of the model decreases as the number of epochs increases, as illustrated by the epoch versus loss curve in Fig. 8. Thus, the TRI-FH approach is expected to have an accuracy of 98.07 %.

4.2. COMPARATIVE ANALYSIS

A comparative analysis between the proposed model and the existing machine models is done in this section.

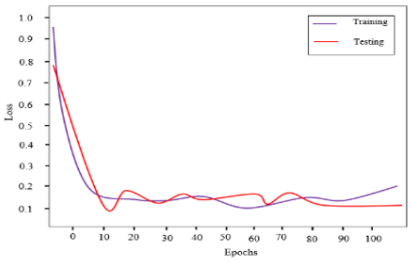

Fig. 8 – Training and testing loss curve of proposed TRI-FH model.

The performance of the current methods was compared using precision, specificity, recall, accuracy, and F1 score to show that the suggested strategy's outcome is more effective. The overall performance of machine learning models is compared with the recommended method in Table 2. A comparison of the suggested model with machine learning networks, such as ResNet, DenseNet, LinkNet, and U-Net, is shown in Table 2.

Table 2
Comparative analysis of existing deep learning networks with the proposed TRI-FH model

Networks	**Accuracy**	**Specificity**	**Precision**	**Recall**	**F1 Score**
ResNet	95.64	93.47	92.82	89.76	90.64
DenseNet	97.82	96.24	94.45	90.28	89.24
LinkNet	93.21	90.47	86.34	85.86	88.89
Unet	95.67	93.64	87.47	83.78	92.87
TRI-FH approach	98.07	96.46	94.62	91.69	90.53

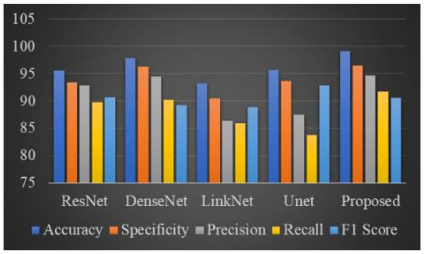

Fig. 9 – Comparison of existing deep learning networks with the proposed TRI-FH model.

Table 3
Comparison of existing versus proposed TRI-FH model

Authors	Methods	Accuracy
Masaaki [16]	CNN	89.1%
Imayanmosha [19]	Machine Learning	95.33%
Zamzmi [24]	Deep learning	91.6%
Proposed	TRI-FH approach	98.07%

The proposed TRI-FH approach improves the overall accuracy of the ResNet, DenseNet, LinkNet and U-Net is 95.64 %, 97.82 %, 93.21 %, and 95.6 7% respectively. This approach improves the overall recall of the ResNet, DenseNet, LinkNet, and U-Net is 89.76 %, 90.28 %, 85.86 %, and 83.78 % respectively. The proposed TRI-FH improves the overall F1 score of the ResNet, DenseNet, LinkNet and U-Net is 90.64 %,89.24 %, 88.89 %, and 90.53 % respectively. Based on the network parameters (Fig. 9), the suggested network's efficiency is evaluated. Table 3 shows that, in comparison to CNN, machine learning, and deep learning,

respectively, the proposed TRI-FH approach improves overall accuracy by 89.1 %, 95.33 %, and 91.6 %. It presents a comparison between the various methods' algorithms. The average accuracy value is 98.07 %, as can be seen in the table, indicating that the TRI-FH yields higher accuracy values.

4. **CONCLUSION**

In this paper, the gathered 3D echo images are pre-processed to improve the quality of the images. The classified TR cases are fed to the segmentation phase for segmenting the affected valve of the fetus. The experimental TRI-FH approach achieves a total accuracy of 98.07 %. The proposed TRI-FH method performs better in terms of accuracy, precision, recall, specificity, and F1 score when compared to current methods. The proposed TRI-FH method performs better in terms of accuracy, precision, recall, specificity, and F1 score when compared to current methods. The proposed TRI-FH model improves the overall accuracy by 95.64 %, 97.82 %, 93.21 %, and 95.67 % better than ResNet, DenseNet, LinkNet, and U-Net respectively. To enhance the model's performance, we employ transfer learning by fine-tuning a pre-trained neural network architecture on our specific dataset. The integration of attention mechanisms further improves the model's ability to focus on relevant regions within the 3D echo images, increasing sensitivity and reducing false positives. In the future, 3D echo images can be visualized using several techniques to highlight human-recognizable clinical features.

ACKNOWLEDG(E)MENTS

The authors would like to thank the reviewers for all their careful, constructive, and insightful comments concerning this work.

Received on 24 March 2023

REFERENCES

1. F. Barbieri, M. Schröder, N. Beyhoff, U. Landmesser, M. Reinthaler, M. Kasner, *Percutaneous edge-to-edge tricuspid valve repair in a patient with Cor Triatriatum dexter: a case report,* Journal of Cardiovascular Development and Disease, **8**, *9*, p. 111 (2021).
2. C.H. Lee, D.W. Laurence, C.J. Ross, K.E. Kramer, A.R. Babu, E.L. Johnson, M.C. Hsu, A. Aggarwal, A. Mir, H.M. Burkhart, R.A. Towner, *Mechanics of the tricuspid valve – From clinical diagnosis/treatment, in-vivo and in-vitro investigations, to patient-specific biomechanical modelling,* Bioeng., **6**, *2*, p. 47 (2019).
3. E. Dzilic, T. Guenther, A. Bouziani, B. Voss, S. Voss, K. Vitanova, M. Krane, R. Lange, *results after repair of functional tricuspid regurgitation with a three-dimensional annuloplasty ring,* J. Clin. Med, **10**, *21*, p. 5080 (2021).
4. D. Munteanu, C. Bejan, N. Munteanu, C. Zamfir, M.Vasić, S.M. Petrea, D. Cristea, *Deep-learning-based system for assisting people with Alzheimer's disease*, Electronics, **11**, *19*, p. 3229 (2022).
5. H. Gupta, P. Kumar, S. Saurabh, S.K. Mishra, B. Appasani, A. Pati, C. Ravariu, and A. Srinivasulu, *Category boosting machine learning algorithm for breast cancer prediction,* Rev. Roum. Sci. Techn. – Électrotechn. et Énerg., **66**, *3*, pp. 201–206 (2021).
6. Z. Rguibi, A. Hajami, D. Zitouni, A. Elqaraoui, A. Bedraoui, *Cxai: explaining convolutional neural networks for medical imaging diagnostic,* Electronics, **11**, *11*, p. 1775 (2022).
7. A. Topor, D. Ulieru, C. Ravariu, F. Babarada, *Development of a new one-eye implant by 3D bioprinting technique*, Rev. Roum. Sci. Techn. – Électrotechn. et Énerg., **68**, *2*, pp. 247–250 (2023).
8. R.T. Hahn, J.D. Thomas, O.K. Khalique, J.L. Cavalcante, F. Praz, W.A. Zoghbi, *Imaging assessment of tricuspid regurgitation severity*, JACC: Cardiovasc. Imaging, **12**, *3*, pp. 469–490 (2019).
9. L.P. Badano, R. Hahn, H. Rodríguez-Zanella, D. Araiza Garaygordobil, R.C. Ochoa-Jimenez, D. Muraru, *Morphological assessment of the tricuspid apparatus and grading regurgitation severity in patients with functional tricuspid regurgitation: thinking outside the box*, JACC: Cardiovasc. Imaging, **12**, *4*, pp. 652–664 (2019).
10. Q.W. Jin, A.B.M. Ghazi, J. Kolanthaivelu, S.A. Yahaya, *Novel treatment of atrial functional tricuspid regurgitation using transcatheter bicaval valve implantation (TricValve)*, Asia Intervention, **8**, *2*, p. 138 (2022).
11. S. Gogoneaţă, C. Mărculescu, A.M. Morega, *Characterization of electrical properties of 3d printed biosensors with various electrode geometries*, Rev. Roum. Sci. Techn. – Électrotechn. et Énerg., **68**, *2*, pp. 241–246 (2023).
12. M. Penso, M. Pepi, L. Fusini, M. Muratori, C. Cefalù, V. Mantegazza, P. Gripari, S.G. Ali, F. Fabbiocchi, A.L. Bartorelli, E.G. Caiani, *Predicting long-term mortality in TAVI patients using machine learning techniques*, Journal of Cardiovascular Development and Disease, **8**, *4*, p. 44 (2021).
13. G. Italiano, L. Fusini, V. Mantegazza, G. Tamborini, M. Muratori, S. Ghulam Ali, M. Penso, A. Garlaschè, P. Gripari, M. Pepi, *Novelties in 3D transthoracic echocardiography*, J. Clin. Med. Res, **10**, *3*, p. 408, (2021).
14. M. Glavaški, A. Preveden, Đ. Jakovljević, N. Filipović, L. Velicki, *Subtypes and Mechanisms of Hypertrophic Cardiomyopathy Proposed by Machine Learning Algorithms*, Life, **12**, *10*, p. 1566, (2022).
15. C. Chao, H.L. Wu, A. Seri, A. Shanbhag, C. Rayfield, Y. Wang, S. Smith, F.D. Fortuin, J. Sweeney, M.F. Eleid, M. Alkhouli, *Unsupervised machine learning clustering identifies phenotypes of optimal candidates in mitraclip patients*, Circ., **144** (Suppl. 1), A10680-A10680 (2021).
16. H. Nisar, D. Fakim, D. Bainbridge, E. Chen, T. Peters, *3D localization of vena contracts using Doppler ICE imaging in tricuspid valve interventions*, International J. Comput. Assisted Radiol. Surg., **1-9** (2022).
17. M. Komatsu, A. Sakai, R. Komatsu, R. Matsuoka, S. Yasutomi, K. Shozu, A. Dozen, H. Machino, H. Hidaka, T. Arakaki, K. Asada, *Detection of cardiac structural abnormalities in fetal ultrasound videos using deep learning*, Appl. Sci., **11,** *1*, 371.
18. Wahlang, A.K. Maji, G. Saha, P. Chakrabarti, M. Jasinski, Z. Leonowicz, E. Jasinska, *Deep learning methods for classification of certain abnormalities in echocardiography*, Electron., **10**, *4*, p. 495 (2021).
19. S. Sengan, A. Mehbodniya, S. Bhatia, S.S. Saranya, M. Alharbi, S. Basheer, V. Subramaniyaswamy, *Echocardiographic image segmentation for diagnosing fetal cardiac rhabdomyoma during pregnancy using deep learning*, IEEE Access, **10**, 114077-114091 (2022).
20. Wahlang, S.M. Hassan, A.K. Maji, G. Saha, M. Jasinski, Z. Leonowicz, E. Jasinska, *Classification of valvular regurgitation using echocardiography*, Appl. Sci., **12**, *20*, p. 10461 (2022).
21. N. Bouchahda, R. Ayari, R. Wei, W. Majewski, N. Bouchahda, *Study of cardiac fluid dynamics in the right side of the heart with AI PIV*, 75th Annual Meeting of the APS Division of Fluid Dynamics, APS DFD 2022 Indianapolis, Indiana, USA, 2022.
22. N. Khatib, A. Gover, R. Beloosesky, Y.Ginsberg, Weiner, Z., Eigenberg, S. and Bronshtein, M., *Early prenatal diagnosis of tricuspid valve dysplasia*, The Journal of Maternal-Fetal & Neonatal Medicine, **35**, *2*, pp. 410–413 (2022).
23. D.R. Florescu, D. Muraru, V. Volpato, M. Gavazzoni, S. Caravita, M.Tomaselli, P. Ciampi, C. Florescu, T.A. Bălşeanu, G. Parati, L.P. Badano, *Atrial functional tricuspid regurgitation as a distinct pathophysiological and clinical entity: no idiopathic tricuspid regurgitation anymore*, J. Clin. Med., **11**, *2*, p. 382 (2022).
24. J.J. Silbiger, *Atrial functional tricuspid regurgitation: an underappreciated cause of secondary tricuspid regurgitation.* Echocardiography, **36**, *5*, pp. 954–957 (2019).
25. G. Zamzmi, L.Y. Hsu, W. Li, V. Sachdev, S. Antani, *Echo Doppler flow classification and goodness assessment with convolutional neural networks*, 18th IEEE International Conference on Machine Learning and Applications (ICMLA), 2019, pp. 1744–1749.
26. M. Majmundar, A. Kumar, R. Doshi, P. Shah, S. Arora, M. Shariff, D. Adalja, F. Visco, H. Amin, S. Vallabhajosyula, N. Gullapalli, *Meta-analysis of transcatheter aortic valve implantation in patients with stenotic bicuspid versus tricuspid aortic valve*, American Journal of Cardiology, **145**, pp. 102–110 (2021).